UC Berkeley

UC Berkeley Previously Published Works

Title

Dynamic Remodeling of the Magnetosome Membrane Is Triggered by the Initiation of Biomineralization

Permalink

https://escholarship.org/uc/item/8vz112gg

Journal

mBio, 7(1)

ISSN

2161-2129

Authors

Cornejo, Elias
Subramanian, Poorna
Li, Zhuo
et al.

Publication Date

2016-03-02

DOI

10.1128/mbio.01898-15

Peer reviewed

eScholarship.org Powered by the California Digital Library
University of California

AMERICAN SOCIETY FOR MICROBIOLOGY | mBio®

RESEARCH ARTICLE

Dynamic Remodeling of the Magnetosome Membrane Is Triggered by the Initiation of Biomineralization

Elias Cornejo,[a] Poorna Subramanian,[b] Zhuo Li,[b]* Grant J. Jensen,[b] Arash Komeili[a]

Department of Plant and Microbial Biology, University of California, Berkeley, California, USA[a]; Division of Biology and Biological Engineering, California Institute of Technology, Pasadena, California, USA[b]

* Present address: Zhuo Li, City of Hope, Los Angeles, California, USA.

ABSTRACT **Magnetotactic bacteria produce chains of membrane-bound organelles that direct the biomineralization of magnetic nanoparticles. These magnetosome compartments are a model for studying the biogenesis and subcellular organization of bacterial organelles. Previous studies have suggested that discrete gene products build and assemble magnetosomes in a stepwise fashion. Here, using an inducible system, we show that the stages of magnetosome formation are highly dynamic and interconnected. During *de novo* formation, magnetosomes first organize into discontinuous chain fragments that are subsequently connected by the bacterial actin-like protein MamK. We also find that magnetosome membranes are not uniform in size and can grow in a biomineralization-dependent manner. In the absence of biomineralization, magnetosome membranes stall at a diameter of ~50 nm. Those that have initiated biomineralization then expand to significantly larger sizes and accommodate mature magnetic particles. We speculate that such a biomineralization-dependent checkpoint for membrane growth establishes the appropriate conditions within the magnetosome to ensure successful nucleation and growth of magnetic particles.**

IMPORTANCE **Magnetotactic bacteria make magnetic nanoparticles inside membrane-bound organelles called magnetosomes; however, it is unclear how the magnetosome membrane controls the biomineralization that occurs within this bacterial organelle. We placed magnetosome formation under inducible control in *Magnetospirillum magneticum* AMB-1 and used electron cryo-tomography to capture magnetosomes in their near-native state as they form *de novo*. An inducible system provided the key evidence that magnetosome membranes grow continuously unless they have not properly initiated biomineralization. Our finding that the size of a bacterial organelle impacts its biochemical function is a fundamental advance that impacts our perception of organelle formation and can inform future attempts aimed at creating designer magnetic particles.**

Received 2 November 2015 **Accepted** 20 January 2016 **Published** 16 February 2016

Citation Cornejo E, Subramanian P, Li Z, Jensen G, Komeili A. 2016. Dynamic remodeling of the magnetosome membrane is triggered by the initiation of biomineralization. mBio 7(1):e01898-15. doi:10.1128/mBio.01898-15.

Editor Yves V. Brun, Indiana University

Copyright © 2016 Cornejo et al. This is an open-access article distributed under the terms of the Creative Commons Attribution-Noncommercial-ShareAlike 3.0 Unported license, which permits unrestricted noncommercial use, distribution, and reproduction in any medium, provided the original author and source are credited.

Address correspondence to Arash Komeili, komeili@berkeley.edu.

Organelles are dynamic—their structure, composition, subcellular localization, and internal biochemical environment can change in response to cellular demands (1–4). Bacteria possess a number of specialized protein-bound and membrane-bound compartments that can be vital for their survival in nature (5, 6). Similar to eukaryotes, some bacterial organelles are dynamic, undergo structural and compositional remodeling, and require proper subcellular organization for faithful segregation among daughter cells (7–13). However, the molecular mechanisms of membrane remodeling to achieve distinct morphologies, regulate size, and segregate organelles in bacteria are not well understood.

Magnetotactic bacteria (MTB) produce membrane-bound compartments called magnetosomes that direct the formation of magnetic nanoparticles (14). Individual magnetosomes are organized into one or more chains that allow the cell to orient and navigate along geomagnetic fields (15–17). A series of previous biochemical, genetic, and comparative genomic studies have identified a number of factors required for the formation and activity of magnetosomes (18–26). These analyses have led to a stepwise model for the assembly and function of magnetosomes in which membrane biogenesis, chain formation, and biomineralization constitute distinct and separable stages (23, 24). Since this view is generated from static snapshots of mutant phenotypes, the spatiotemporal dynamics that might link the sequential stages of compartmentalization and biomineralization remain unexplored. For instance, it is unclear if the magnetosome membrane forms from a single-step deformation of the inner cell membrane or if it can dynamically expand throughout its development. There are also controversies regarding the molecular and physical mechanisms that create a chain of magnetosomes. Some studies have implicated magnetic interactions in magnetosome chain organization, while others have not (23, 24, 27–29). Finally, it is unclear if the biochemical activity of the organelle in producing a magnetic biomineral influences its cell biological characteristics.

To address these outstanding issues, we designed a system to have inducible control over magnetosome membrane formation in *Magnetospirillum magnetotacticum* AMB-1. We show that magnetosomes formed in the absence of a preexisting chain initially

have a discontinuous, but long-range alignment. The discontinuities in the chain are eventually corrected in a manner that is dependent on the bacterial actin-like protein MamK. Surprisingly, we also find that individual magnetosome membranes show a dynamic two-step growth pattern. In the first step, a nascent magnetosome membrane is remodeled from the inner cell membrane but does not grow beyond ~50 nm. A magnetosome membrane can continue to the second step of growth if, and only if, it has initiated biomineralization. We speculate that such a biomineralization checkpoint creates the proper environment for the formation of mature magnetite particles.

RESULTS

Magnetosome formation can be placed under inducible control. In order to control magnetosome formation, we sought to complement a mutant strain incapable of producing magnetosomes with its missing gene in an inducible fashion. In AMB-1, four genes appear to be necessary, but not sufficient, to make the magnetosome membrane compartment: *mamI*, *mamL*, *mamQ*, and *mamB* (23). We screened N-terminal and C-terminal M2-tagged versions of each of these required genes and found that M2-tagged *mamQ* could restore the magnetic phenotype of the Δ*mamQ* Δ*R9* genetic background (LD9ΔQ) that lacks both functional copies of *mamQ* (see Fig. S1D in the supplemental material). To ensure full repression of the inducible gene, *mamQ*-M2 was placed under the control of a combination of a LacI-repressed promoter and a translationally repressed synthetic riboswitch (see Fig. S1A) (30). Additionally, the copy number of the inducible construct was reduced by integration into a neutral site in the chromosome. In this context, the expression of *mamQ*-M2 and magnetosome formation was successfully repressed in the LD9ΔQ strain (see Fig. S1A). Western blotting using antibodies against the M2 tag shows that no detectable MamQ-M2 is produced in the absence of the inducers and that maximal induction occurs when both inducers IPTG (isopropyl-β-D-thiogalactopyranoside) and theophylline are introduced (see Fig. S1B and S1C). In this configuration, the riboswitch appears to be a more potent inhibitor since it is required to repress leaky transcription from *lacI* even when both constructs are integrated into the chromosome (see Fig. S1C).

Magnetosome formation in the inducible strain (referred to as Q_{Ind} for simplicity) was assessed by monitoring chain formation and the development of a cellular magnetic response. The localization of a magnetosome protein, MmsF, fused to green fluorescent protein (GFP-MmsF) was used to visualize the development of magnetosome chains during induction. MmsF is a 124-amino-acid transmembrane protein of unknown function that has been shown to control the size and shape of magnetic particles in AMB-1 (25, 31). GFP-MmsF complements the small-crystal phenotype of the *mmsF* deletion strain (25). Furthermore, GFP-MmsF localizes to the magnetosome chain in both wild-type and Δ*mmsF* strains and uniformly around the cytoplasmic membrane in strains that are incapable of making magnetosomes (25). We integrated *gfp-mmsF* into the chromosome of the Q_{Ind} strain by allelic replacement of the native copy of *mmsF*. In the uninduced state, GFP-MmsF localizes uniformly around the inner membrane in the Q_{Ind} strain. However, GFP-MmsF gradually acquires a linear localization pattern when Q_{Ind} is induced for 6 h (Fig. 1A and B). The first change in the localization pattern is observed at 2 h postinduction (hpi), where 44% ± 9% of the cell population has unaligned foci of GFP-MmsF and 18% ± 4% of the population has aligned foci (Fig. 1A and B). At 3 hpi, the percentage of cells with a linear localization pattern of GFP-MmsF, either aligned foci or solid lines, increases to 46% ± 13% (Fig. 1A and B). By 6 hpi, 86% ± 9% of the population displays a linear localization pattern of GFP-MmsF (Fig. 1A and B). In addition, we assessed if the induced magnetosomes were functional by measuring the coefficient of magnetism (C_{mag}) of the cell culture over time

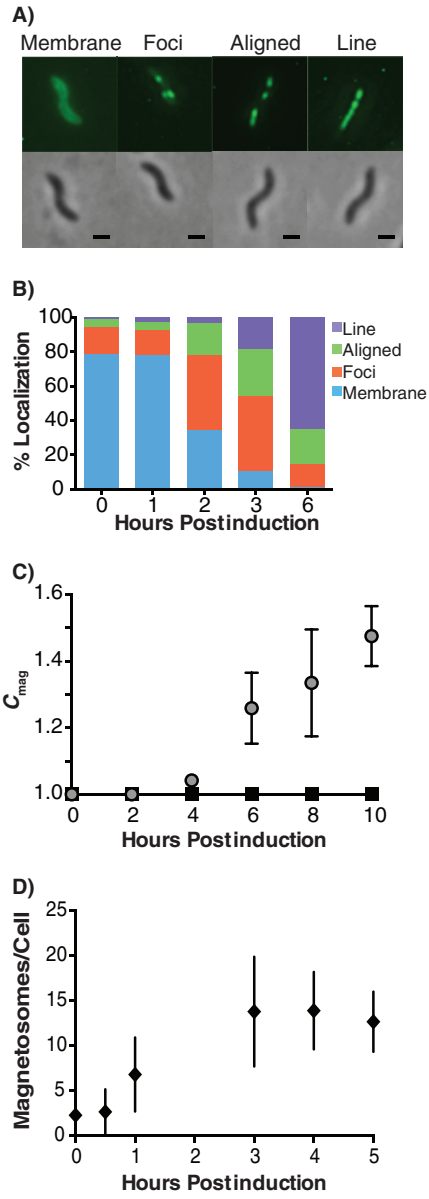

FIG 1 Magnetosome formation can be placed under genetically inducible control to follow *de novo* magnetosome formation and organization. (A) GFP-MmsF can be classified into 4 distinct localization patterns: membrane localized, unaligned foci, aligned foci, and a solid line (scale bars, 500 nm). (B) Mean localization patterns of GFP-MmsF for three independent 6-h induction time courses. (C) Magnetite crystal formation is assessed by the degree of magnetic response (C_{mag}) of triplicate cell culture induced over a 10-h time course. (D) Quantification of the mean number of magnetosomes per cell that could be visualized by electron crytomography (ECT) over a 5-h time course. Seven to 10 tomograms of the induced cell population were reconstructed for each time point.

(Fig. 1C). This measurement relies on the differential light-scattering properties of a culture as cells are aligned perpendicular or parallel relative to the light beam via an external magnetic field. Uninduced cultures were nonmagnetic but could be induced to have a weak magnetic response at 4 hpi, which drastically increased by 6 hpi (Fig. 1C). Consistent with these measurements, transmission electron microscopy (TEM) confirmed the development of mature magnetosome chains during the time course experiment (see Fig. S1E). Taken together, these results show that magnetosome formation can be placed under inducible control and that the developmental stages of chain formation and biomineralization can be monitored over time.

The combination of GFP-MmsF imaging and C_{mag} measurements implies that magnetosome membranes are most likely formed early in the time course experiment prior to the development of magnetic biominerals. In order to visualize these early membrane dynamics at a high resolution, we performed electron cryotomography (ECT) on cells sampled throughout the induction time course. In previous work, wild-type-like assemblies of empty magnetosome membranes were absent from LD9ΔQ cells that were chemically fixed, sectioned, and imaged by conventional TEM (23). However, in ECT imaging cellular membranes and subcellular structures are very well preserved in a near-native state, eliminating artifacts that arise from chemical fixing or sectioning (32, 33). In the LD9ΔQ strain, we observe structures that have some magnetosome-like characteristics (see Fig. S2 in the supplemental material). Similar to magnetosomes, these structures can be membrane bound and in rare cases even contain electron-dense particles reminiscent of early biomineralization. However, these structures are also distinct from magnetosomes since they occur mostly in isolation, lack fully formed magnetic crystals, and are not flanked by filaments. Since it cannot be ruled out that these structures are magnetosomes, we imposed strict criteria to positively identify magnetosomes versus other membrane structures. Therefore, for the rest of the ECT work presented here, a feature was only included in the analysis if it was connected or in close proximity to the inner membrane and if it was adjacent to other structures resembling magnetosomes. These criteria allowed us to distinguish magnetosomes that are being assembled into a chain from background cytoplasmic vesicles, misaligned magnetosomes, and other inner membrane features that may also be present in the cell.

Despite the presence of isolated cytoplasmic membrane structures under the uninduced condition, we observed an increase in the number of magnetosomes within the cell at 1 hpi (Fig. 1D). In bacteria, subcellular organization is oftentimes achieved by directing proteins and processes to particular cellular locations, such as the cell pole or the midcell (34). However, we were not able to discern any distinct or dedicated sites of magnetosome biogenesis. Thus, in the context of the inducible system, the machinery required to form the magnetosome compartment may be distributed at multiple sites throughout the inner membrane.

Magnetosome chain organization: alignment pattern and chain continuity. In addition to investigating the morphology and spatial organization of early magnetosome formation events, we used the inducible system to define the pattern, dynamics, and molecular requirements for chain formation over time. To better define the temporal properties and dynamics of chain formation during the induction, we determined the distance between adjacent magnetosomes to derive a quantitative measure of chain continuity. In wild-type cells, the average edge-to-edge distance between adjacent magnetosomes is 28.7 nm, and only 5.4% of distances exceed 75 nm (see Fig. S3 in the supplemental material). Based on our observations of magnetosome spacing in the wild type, an intermagnetosome measurement was considered a gap if its edge-to-edge distance exceeded 75 nm. When magnetosome formation was induced in the Q_{Ind} strain, clearly aligned but discontinuous chains of magnetosomes were observed at 3 hpi (Fig. 2A). The average distance between adjacent magnetosomes is 64.6 nm, and 21.6% of distances constitute a gap (Fig. 2C). Over time, the number of gaps in Q_{Ind} decreases to essentially wild-type levels and only 5.1% of distances are gaps at 5 hpi (Fig. 2A and C). These findings show that in the absence of a preexisting chain, clusters of magnetosomes are separated by a number of gaps but still maintain a long-range alignment across the cell. These discontinuities are then closed to form a magnetosome chain.

Previous studies have shown that in AMB-1, the loss of *mamK* results in a chain organization defect where gaps between adjacent magnetosomes occur within the chain (35). MamK forms dynamic filaments *in vivo* and *in vitro* in an ATP-dependent manner, but the exact role of MamK in chain organization is unclear (36, 37). In order to better understand the role of MamK in magnetosome chain formation, we deleted *mamK* in the inducible strain (creating Q_{Ind}ΔK) and induced magnetosome formation to observe *de novo* chain assembly. Much like induction of magnetosome formation in the Q_{Ind} background, a clear chain of aligned magnetosomes with a number of gaps is visible at 3 hpi (Fig. 2B). These gaps account for 42.6% of the intermagnetosome distances measured in the population (Fig. 2C). Unlike the induced Q_{Ind} strain, however, in which these gaps eventually disappear, the Q_{Ind}ΔK strain still retains large gaps in the magnetosome chain (Fig. 2B and D). Indeed, at 5 hpi 39.2% of the pairwise distances measured between adjacent magnetosomes are still gaps (Fig. 2C).

These results suggest that two distinct organizational principles govern magnetosome chain formation: magnetosome alignment and chain continuity. Alignment is a long-range mechanism to establish an axis for the magnetosome chain, whereas chain continuity is a short-range mechanism that closes the gaps between two adjacent magnetosomes. Alignment appears to occur first, in a manner that is independent of *mamK*. Once long-range alignment is established, the gaps between adjacent magnetosomes are closed in a manner that is dependent on *mamK*. We speculate that MamK could act to fill the gaps through guiding the direct synthesis of new magnetosomes within the gaps, recruiting existing but misaligned magnetosomes to the gaps, or by physically pulling adjacent magnetosomes together to close the gaps. Real-time microscopy techniques that independently track newly formed magnetosomes versus preexisting magnetosomes could potentially distinguish between these different models and elucidate how MamK closes gaps to form a continuous magnetosome chain.

There are likely additional forces involved in the subcellular organization of magnetosomes that remain to be discovered. It has been proposed that the magnetic interactions between magnetosomes could facilitate chain formation, since induction of biomineralization in a closely related magnetotactic bacterium, *Magnetospirillum gryphiswaldense* MSR-1, results in a rapid reorganization of magnetosomes into a chain (27). Since *de novo* chain formation occurs within 5 h of the induction time course, when only 3% of the magnetosomes contain magnetic particles, it is

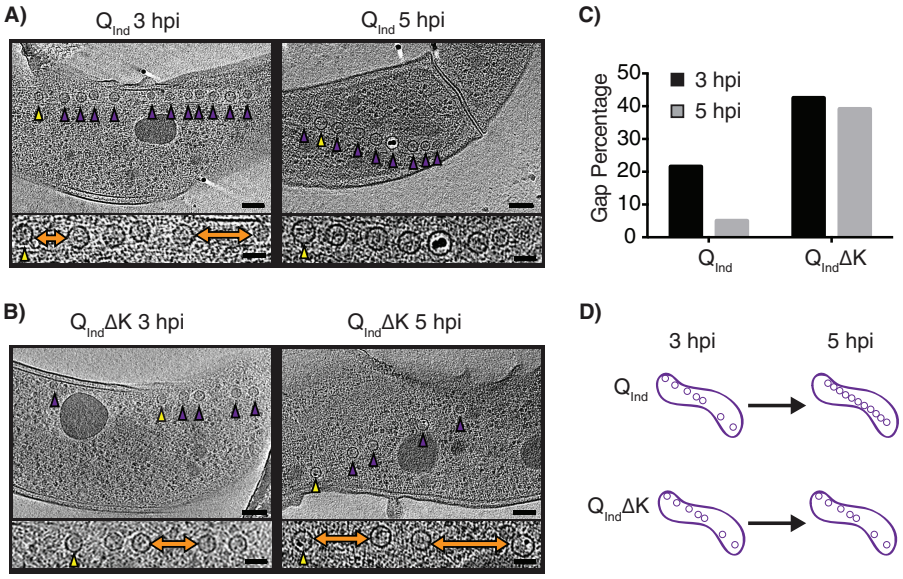

FIG 2 MamK is required for chain continuity but not long-range alignment. (A and B) Representative ECT images of long-range alignment of the magnetosome chain at 3 hpi and 5 hpi for Q_{Ind} and Q_{Ind}ΔK, respectively (scale bars, 100 nm). The inset is a higher magnification of the same cell to show where gaps occur in the chain (scale bars, 50 nm). Gaps are denoted by double-sided orange arrows. A yellow arrowhead denotes the same magnetosome at each magnification for reference. Purple arrowheads point to individual magnetosomes in the chain. (C) Quantification of the number of gaps found in magnetosome chains of induced Q_{Ind} and Q_{Ind}ΔK at 3 hpi and 5 hpi. The gap percentage is the percentage of edge-to-edge distances between adjacent and aligned magnetosomes that are >75 nm in length. The total numbers of edge-to-edge distances measured (*n*) for each time point are as follows: Q_{Ind} 3 hpi, $n = 74$; Q_{Ind} 5 hpi, $n = 99$; Q_{Ind}ΔK 3 hpi, $n = 94$; and Q_{Ind}ΔK 5 hpi, $n = 97$. (D) Cartoon depicting magnetosome chain organization in Q_{Ind} versus Q_{Ind}ΔK. At 3 hpi, both strains exhibit long-range but discontinuous magnetosome alignment. At 5 hpi, the Q_{Ind} strain has filled these gaps, whereas Q_{Ind}ΔK does not fill the chain discontinuities.

clear that magnetic interactions between magnetosomes are not required to form a magnetosome chain in AMB-1 (Fig. 2A and B). Even though other candidate cytoskeletal proteins, such as FtsZ-like and MamK-like, exist in AMB-1, we did not find magnetosome-associated filaments in the absence of MamK or between distantly aligned magnetosomes in the Q_{Ind} strain by ECT (38–40). A long-range alignment factor or combination of factors therefore remains to be discovered.

Magnetosome membrane compartments are dynamic structures that can increase in size. It is not known if the size of the membrane ultimately determines the size of the crystal or if the growth of the mineral can lead to a change in membrane size. One possibility is that one-step remodeling of the cytoplasmic membrane creates a magnetosome membrane compartment of a predetermined size that provides the ultimate boundaries to control the size of the growing mineral. Alternatively, the magnetosome membrane could expand continuously in conjunction with a growing crystal. By examining the size of magnetosomes in the Q_{Ind} induction time course experiment, we find that at 1 hpi, magnetosome membrane diameter has an approximately normal distribution with a mean of 29.4 ± 5.0 nm (Fig. 3A; see Table S1 in the supplemental material). This distribution shifts to 38.5 ± 5.5 nm at 3 hpi and then again to 42.4 ± 5.2 nm at 5 hpi (Fig. 3A; see Fig. S4A and Table S1 in the supplemental material). Based on two independent statistical analyses, Student's *t* test and Mann-Whitney *U* test, there are significant increases in both the mean and median of the membrane size distributions from 1 to 3 hpi ($P < 1E-05$) and from 3 to 5 hpi ($P < 0.05$) (see Table S2 in the supplemental material) (41). A shift in the entire distribution at each time point suggests that the increases in size are not due to the one-step production of larger magnetosomes at later time points (Fig. 3A; see Fig. S4A and Table S1). Instead, these results strongly argue that magnetosomes continually increase in size after the initial membrane invagination event.

The observations of magnetosome membrane growth in the inducible system prompted us to search for evidence of this dynamic behavior in wild-type cells. Indeed, when wild-type cells at steady state were imaged by ECT, a range of magnetosome membrane sizes from roughly 20 to 70 nm were observed (Fig. 3B). Curiously, magnetosomes that lacked electron-dense nanoparticles did not exceed ~50 nm in diameter (Fig. 3B; see Fig. S4A and Table S1 in the supplemental material). These smaller empty magnetosome membranes could represent defective compartments incapable of supporting biomineralization, or they may hint at a link between magnetite formation and membrane growth. To distinguish between these possibilities, we compared membrane size distributions in wild-type cultures grown under iron-rich conditions (+Fe) to those cultivated under iron-poor conditions (−Fe) (Fig. 3C). In previous studies, we have shown than under –Fe conditions, nearly all magnetosomes are devoid of magnetite particles (28, 35). These empty magnetosomes are functional for biomineralization since a shift to +Fe conditions results in rapid initiation of magnetite formation within them (22, 28). Interestingly, the mean diameter of −Fe magnetosomes (38.2 ± 4.7 nm) is significantly smaller than the mean diameter of +Fe magnetosomes (48.5 ± 11.7 nm) ($P < 1E-05$) (Fig. 3C; see Tables S1 and S2 in the supplemental material). In fact, in the –Fe cells no magnetosome membranes were larger than 55 nm, whereas the +Fe cells had magnetosomes ranging in size from 21 to 79 nm (Fig. 3C; see Table S1). Taken together, these findings suggest that magnetosomes that have not initiated crystal formation are limited in size

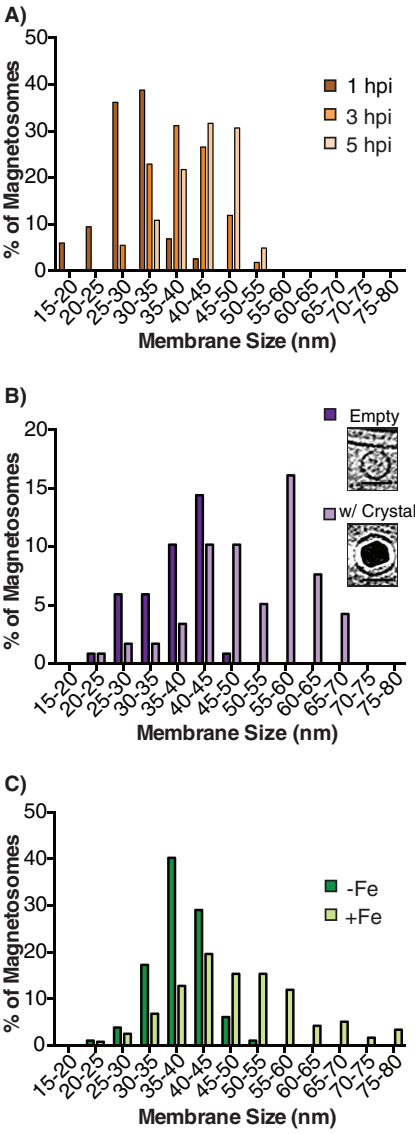

FIG 3 Magnetosome membranes grow in diameter in a manner that is dependent on their biomineralization state. (A) Distribution of magnetosome size at three points in the induction time course of Q_{Ind}: 1 hpi ($n = 116$), 3 hpi ($n = 110$), and 5 hpi ($n = 101$). (B) Distribution of magnetosome size in wild-type AMB-1 ($n = 117$). Shown are representative images of an empty magnetosome versus a magnetosome with crystal (scale bars, 50 nm). (C) Magnetosome membrane size distribution in wild-type AMB-1 grown in either iron-rich (+Fe; $n = 117$) or iron-poor (−Fe; $n = 172$) medium. Membrane size is an average of 3 independent diameter measurements of the same magnetosome at the tomographic slice where it is largest and most visible. The number of magnetosomes measured is *n*.

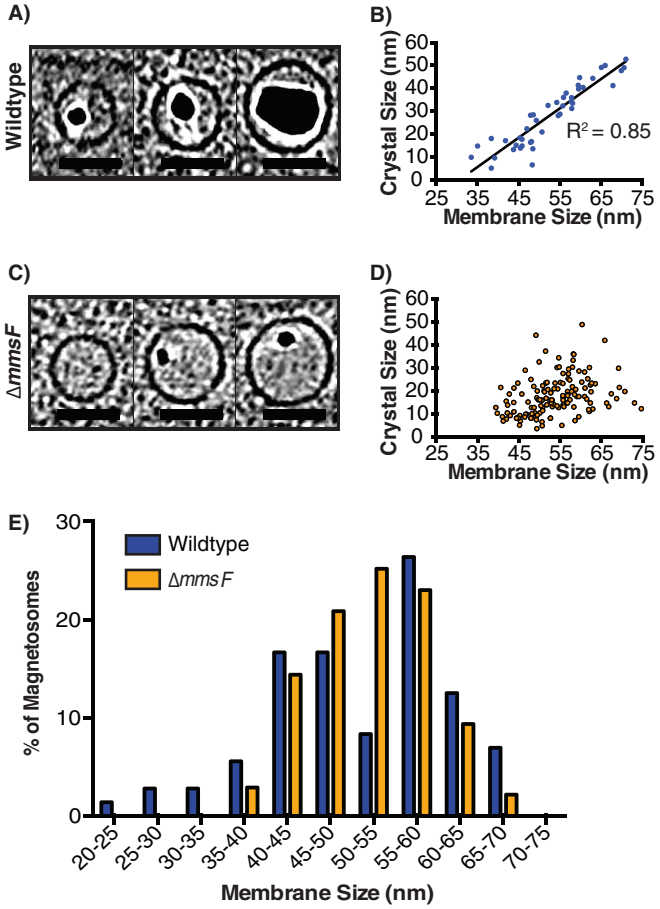

FIG 4 Crystal growth does not physically expand the magnetosome membrane. (A) Representative ECT images of magnetosomes of different sizes in wild-type AMB-1 (scale bars, 50 nm). (B) Scatterplot and regression analysis of membrane size versus crystal size for magnetosomes that harbor crystals in wild-type AMB-1 ($n = 72$ magnetosomes). The long axis (crystal length) is reported as crystal size. (C) Representative ECT images of magnetosomes of different sizes in the Δ*mmsF* mutant (scale bars, 50 nm). (D) Scatterplot of membrane size versus crystal size for magnetosomes that harbor crystals in the Δ*mmsF* mutant ($n = 140$ magnetosomes). The long axis (crystal length) is reported as crystal size. (E) Distribution of magnetosome size in the Δ*mmsF* mutant ($n = 243$) compared to wild-type AMB-1 ($n = 117$).

and that biomineralization is required for further membrane expansion.

Curiously, for the magnetosomes that have initiated biomineralization, a linear relationship exists between the size of the magnetosome membrane and the size of its resident crystal, such that the largest magnetosome membranes contain the largest magnetite particles (Fig. 4A and B). Two potential models can be used to explain this observed relationship between magnetosome membrane size and biomineralization. First, it is possible that growth of the mineral physically distends the membrane and provides the force for its expansion beyond ~50 nm. Second, the initiation of biomineralization may be a regulatory cue that signals the expansion of the magnetosome membrane, thus providing a larger space for continued mineral growth. In order to explore if crystal growth physically expands the membrane, we measured the membrane diameter in the Δ*mmsF* biomineralization mutant strain. Previous studies have shown that the Δ*mmsF* mutant makes small crystals whose growth stalls at about 25 nm in length (25). If crystal growth physically expands the magnetosome membrane, then the Δ*mmsF* mutant should have a distribution of membrane diameters that is shifted to the smaller size range. However, in the Δ*mmsF* strain the magnetosome membranes can grow to full size independent of crystal size (Fig. 4C and D). In other words, the magnetosomes that harbor small crystals in the Δ*mmsF* strain can grow as large as magnetosomes in the wild type that harbor mature crystals. The mean size distribution of magnetosome membranes of the Δ*mmsF* mutant (47.9 ± 8.6 nm) is similar to that of the wild

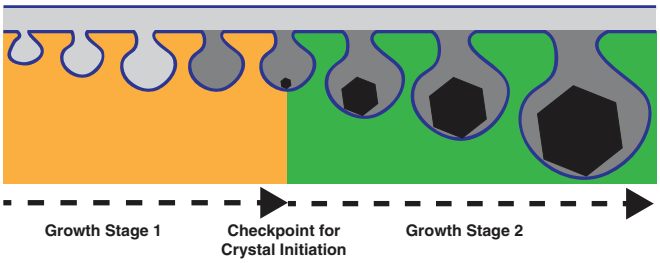

FIG 5 Magnetosome membrane growth is a two-step growth mechanism dependent on biomineralization. The magnetosome membrane compartment is remodeled in two growth stages. In the first stage (orange), the inner membrane is remodeled to form the magnetosome compartment. The magnetosome lumen is most likely similar to that of the periplasm (light gray). Membrane size is restricted until conditions inside the magnetosome membrane are optimal for biomineralization (dark gray). Crystal initiation triggers a second growth stage (green) to accommodate a growing crystal.

type (45.8 ± 11.5 nm) despite its crystal maturation defect (Fig. 4E; see Fig. S4A and Table S1 in the supplemental material). Additionally, similar to the wild type, the empty magnetosomes of the Δ*mmsF* strain are significantly smaller in diameter than the magnetosomes that contain crystals (see Fig. S4B). These results show that the physical forces of the growing crystal are not directly expanding the membrane. Instead, biomineralization triggers a release from a checkpoint that limits magnetosome membrane growth (Fig. 5). This commitment step for the second stage of membrane growth is downstream of crystal initiation but upstream of MmsF activity.

DISCUSSION

Optimizing organelle size is often crucial for its cellular function (42). In eukaryotes, the nucleus and vacuole scale in proportion to cell size, and defects in this scaling result in impaired fitness (42, 43). Likewise, organelles such as mitochondria in yeast and photosynthetic membranes in bacteria can dynamically change their size and morphology to adapt to changing environmental conditions (2, 7). Here, we provide evidence that magnetosomes, a bacterial organelle system, also have mechanisms in place to regulate their size and subcellular positioning in order to properly carry out their cellular function.

Previous studies had suggested that magnetic interaction between neighboring magnetosomes could play a role in organizing the chain (27, 29). These were disputed by findings that cells grown without iron and nonmagnetic mutants still contain intact chains of empty magnetosomes (23, 28). However, it could be argued that the preexisting chain in these cases served as a landmark for the recruitment of empty magnetosomes to the chain. By using an inducible system in a mutant devoid of magnetosomes, we were able to show that chain assembly can be accomplished, *de novo*, without the aid of magnetic interactions. In addition, we identified two time-resolved stages to the chain assembly process. First, several clusters of magnetosomes, separated by large gaps, are aligned over a long range across the long cell axis. Next, with the help of MamK, these gaps are closed to form a full chain.

Much like what we observed here, previous ECT imaging of mutants had shown that in the absence of *mamK*, the magnetosome chain loses its continuity and clusters of magnetosomes are separated by gaps (35, 44). This phenotype could arise as a result of a failure to establish the chain, to maintain it after its formation, or as has been suggested in MSR-1, to properly segregate it across multiple cell divisions (12). However, given the 4- to 6-h doubling time of AMB-1, missegregation events occurring over many cell divisions cannot account for the chain formation defects observed in the absence of *mamK* in the induction experiment. By reconstructing the magnetosome chain *de novo*, we rule out chain segregation as a main driver of the Δ*mamK* mutant phenotype. Instead, we propose two distinct stages of magnetosome chain formation—long-range alignment and chain continuity—and show that *mamK* is required for the latter.

Our most unexpected finding is that the magnetosome membrane grows in a manner that is regulated by a biomineralization-dependent checkpoint. In eukaryotes, a number of membrane remodeling mechanisms exist to achieve the distinct sizes and morphologies of organelles (45–47). The magnetosome membrane does not appear to be remodeled to a fixed size, such as the cargo-specific size of endocytic vesicles generated through clathrin-mediated endocytosis (48). Instead, magnetosomes seem to undergo continuous membrane remodeling, similar to the endoplasmic reticulum and mitochondria (49, 50). It is unclear if the membrane remodeling mechanisms identified in eukaryotes hold true for bacteria. However, we speculate that magnetosomes could grow by insertion or oligomerization of curvature-inducing proteins into the membrane, exchange of material between magnetosomes and the cytoplasmic membrane, or even protein/lipid delivery through fusion with cytoplasmic vesicles. It is also remarkable that throughout its growth, the magnetosome membrane maintains the same overall morphology of a sphere connected to the inner cell membrane through a narrow invagination. This possibly implies the presence of a scaffold that maintains a uniform spherical architecture and perhaps a collar to stabilize the highly curved neck. In eukaryotes, Bin/amphiphysin/Rvs (BAR) domain-containing proteins have been shown to bind and stabilize curved membranes due to their naturally curved domain architecture (46, 51). In AMB-1, *mamY* encodes a putative BAR domain whose deletion results in larger magnetosome membranes (67.9 nm) than those of the wild type (60.1 nm) (52). However, this modest change is size does not appear to impact membrane morphology or biomineralization, and there are likely other factors that control and stabilize magnetosome membrane size and shape.

Finally, the coordination of membrane growth with the onset of biomineralization implies that the size of the organelle is crucial in the development of its final product. It is possible that restricting the volume of the magnetosome lumen provides an efficient means of reaching supersaturated iron levels in order to properly nucleate magnetite (53). Alternatively, as we have speculated previously, a biomineralization-driven checkpoint could result in smaller magnetite particles that are stalled in a superparamagnetic state and unable to commit the organism to a magnetotactic lifestyle (22). Changes under conditions favorable for magnetoaerotaxis would rapidly lead to membrane growth and development of large stable magnets. Our findings in this work have profound consequences for understanding the cell biology of magnetosome organelle formation and the regulation of biomineral formation. Understanding size control and membrane remodeling as it pertains to making magnetic particles within magnetosomes may ulti-

mately lead to a broader understanding of organelle development in other bacterial systems. Additionally, magnetite displays size-dependent changes in its magnetic properties (54). As such, the molecular understanding of membrane size determination will allow for more precise control over the design of synthetic magnetic particles for future industrial applications.

MATERIALS AND METHODS

Bacterial growth and induction conditions. Stock cultures were created from picking single colonies into 1.5 ml of defined minimal media (MG medium) supplemented with 1/100 vol of Wolfe's vitamin solution and 1/100 vol of 3 mM ferric malate as previously described (28). Cultures were incubated at 30°C for 48 h, after which they were moved to room temperature. Stock cultures are good for 1 to 2 weeks at room temperature. Solid medium plates contained 7 g agar per liter of medium. Antibiotics were used at the following concentrations: kanamycin at 15 μg·ml^{-1} in solid medium and 7 μg·ml^{-1} in liquid cultures for strains in which a kanamycin-resistant cassette was integrated into the chromosome.

For anaerobic growth, sealed Balch tubes containing 7 ml of MG medium and 23 ml headspace were autoclaved and flushed with N_2 gas for 10 min. Once cooled to room temperature, 1 ml of 10× ferric malate and 1 ml of 10× Wolfe's vitamin solution were added with a syringe. Finally, 1 ml of inoculum cells was added from a stock culture that was diluted 1:10. The final concentration of iron, vitamins, and cells was 1:100.

Cells were induced with 1 mM theophylline and 1 mM IPTG. Inducer stocks made up of 20 mM theophylline and 40 mM IPTG were prepared by dissolving the appropriate amount of solid inducer into MG medium and sterilized by syringe filtration through a 0.2-μm-pore sterile syringe filter.

C_{mag} time course and growth curve. Cultures were inoculated from 1:100 dilutions of stock culture into sealed Balch tubes as described above. Cultures were incubated at 30°C for approximately 16 to 20 h until the optical density at 400 nm (OD_{400}) of the cultures reached 0.100 to 0.150. Cultures were then passaged into fresh 10-ml sealed Balch tubes in triplicate and incubated at 30°C for an additional 16 to 20 h until they reached an OD_{400} of 0.06. For induction, 750 μl of cell culture was removed and replaced with either 500 μl of 20 mM theophylline and 250 μl of 40 mM IPTG for the induced group or 750 μl of MG medium for the uninduced group.

FM of induction time course. In order to image cells during the induction time course by both fluorescence microscopy (FM) and ECT, the culture volume was scaled up from 10 ml to 100 ml in order to be able to allow for repeated sampling of the cell culture. To inoculate, 100-ml sealed capped Balch bottles containing 90 ml of MG medium were autoclaved and then immediately flushed with N_2 gas for 10 min. One milliliter of 3 mM ferric malate and 1 ml of 100× Wolfe's vitamins were added after the bottles had been cooled to room temperature. The bottles were then inoculated 1:100 from a stock cell culture and incubated at 30°C for approximately 16 to 20 h until the OD_{400} of the culture reached 0.100. To induce, 5 ml of 20 mM theophylline and 2.5 ml 40 mM IPTG were added. In order to avoid overpressurizing the sealed capped bottles, an additional syringe needle was inserted into the rubber stopper while injecting the contents to allow pressure to vent.

To sample, 1 ml of N_2 gas was injected into the bottle and 1 ml of cell culture was removed using the same syringe. The 1-ml cell culture sample was centrifuged at 16,000 × *g* for 3 min, then 750 μl of supernatant was removed, and the remaining 250 μl was centrifuged at 14,000 rpm again to obtain a cell pellet. The medium was removed with a pipette, and the cell pellet was resuspended in 50 μl of MG medium.

Imaging by FM, TEM, and localization pattern quantification. Cells were induced in 100-ml sealed Balch cultures and sampled as described above. To image, 7 μl of resuspended cell pellet sample (sample collection described above) was spotted on an agarose pad containing MG and 1% agarose and allowed to sit on the benchtop for 3 min before placing on the coverslip. The coverslip was then sealed with Valap to prevent desiccation of the agarose pad. Fluorescence microscopy was performed on Nikon Eclipse 80i microscope. Images were acquired at ×1,000 magnification using a QImaging Retiga 2000r Fast 1394 camera. GFP-MmsF localization patterns were quantified using the ImageJ Cell Counter plug-in to score each cell in the field of view according to one of the four distinct localization patterns: membrane, unaligned foci, aligned foci, or solid line (55). The localization patterns for >300 cells were determined for each time point per experiment. For imaging of whole cells by transmission electron microscopy (TEM), 7 μl of resuspended cell pellet sample was absorbed on a 200-mesh Cu grid coated with Formvar film and imaged on a FEI Technai 12 transmission electron microscope equipped with a Gatan Bioscan (1,000 by 1,000) charge-coupled device (CCD) camera model 792 at an accelerating voltage of 120 kV.

Magnetosome membrane and crystal size quantification. Tomogram reconstructions were visualized using the IMOD version 4.7 software developed by the University of Colorado (56). Cells were positioned using the Slicer function to determine magnetosome alignment and orient individual magnetosomes to determine the maximum diameter for magnetosome membrane and crystal. Membrane size is reported as the average of three independent diameter measurements from the orientation where the boundaries of the magnetosome membrane are most visible and the membrane is the largest. Crystal size is reported as the long axis (length) of the crystal.

ECT. For all strains, 1.5 ml of cells was centrifuged at 14,000 × *g* for 3 min to obtain a pellet, which was resuspended in 50 μl of MG medium. Sixteen microliters of resuspended cells was mixed with 4 μl of bovine serum albumin (BSA)-treated 10-nm-diameter colloidal gold fiducial markers (57, 58). Four microliters of this mixture was applied to a glow-discharged, X-thick carbon-coated, R2/2 copper Quantifoil grid (Quantifoil Microtools) in a Vitrobot (FEI Company, Hillsboro, OR). The Vitrobot chamber was maintained at a temperature of 22°C and humidity of 80%. Excess liquid was blotted off the grid with a blot force of 3, blot time of 2.5 s, and drain time of 1 s. The grid was then plunge-frozen in a liquid ethane-propane mixture (59) and imaged by ECT. Imaging was performed on an FEI Polara G2 (FEI Company, Hillsboro, OR) 300-kV field emission gun electron microscope equipped with a Gatan image filter (Gatan, Pleasanton, CA) and K2 Summit counting electron detector camera (Gatan, Pleasanton, CA). Data were collected using the UCSFtomo software (60), with each tilt series ranging from −60° to 60° in 1° increments, an underfocus of 15 μm, and a cumulative electron dose of ~120 e/A^2 or less for each tilt series. The IMOD software package was used to calculate three-dimensional (3D) reconstructions (56).

Plasmids, primers, and strains. Descriptions of the design of all plasmids, primers, and strains used in this study are provided in Text S1 and Tables S3, S4, and S5 in the supplemental material.

SUPPLEMENTAL MATERIAL

Supplemental material for this article may be found at http://mbio.asm.org/lookup/suppl/doi:10.1128/mBio.01898-15/-/DCSupplemental.

Figure S1, PDF file, 2.1 MB.
Figure S2, PDF file, 1.3 MB.
Figure S3, EPS file, 0.7 MB.
Figure S4, EPS file, 1.2 MB.
Table S1, DOCX file, 0.1 MB.
Table S2, DOCX file, 0.1 MB.
Table S3, DOCX file, 0.1 MB.
Table S4, DOCX file, 0.1 MB.
Table S5, DOCX file, 0.1 MB.
Text S1, DOCX file, 0.1 MB.

ACKNOWLEDGMENTS

We thank Dorothée Murat for her intellectual contributions and outstanding mentorship during the early stages of this project.

FUNDING INFORMATION

National Science Foundation (NSF) provided funding to Elias Cornejo under grant number DGE 110640. HHS | NIH | National Institute of General Medical Sciences (NIGMS) provided funding to Elias Cornejo and Arash Komeili under grant number R01GM084122. Howard Hughes Medical Institute (HHMI) provided funding to Poorna Subramanian, Zhuo Li, and Grant J. Jensen.

The funders had no role in study design, data collection and interpretation, or the decision to submit the work for publication.

REFERENCES

1. **Federovitch CM, Ron D, Hampton RY**. 2005. The dynamic ER: experimental approaches and current questions. Curr Opin Cell Biol **17:** 409–414. http://dx.doi.org/10.1016/j.ceb.2005.06.010.
2. **Egner A, Jakobs S, Hell SW**. 2002. Fast 100-nm resolution three-dimensional microscope reveals structural plasticity of mitochondria in live yeast. Proc Natl Acad Sci U S A **99:**3370–3375. http://dx.doi.org/10.1073/pnas.052545099.
3. **Huotari J, Helenius A**. 2011. Endosome maturation. EMBO J **30:** 3481–3500. http://dx.doi.org/10.1038/emboj.2011.286.
4. **Voeltz GK, Barr FA**. 2013. Cell organelles. Curr Opin Cell Biol **25:** 403–405. http://dx.doi.org/10.1016/j.ceb.2013.06.001.
5. **Murat D, Byrne M, Komeili A**. 2010. Cell biology of prokaryotic organelles. Cold Spring Harb Perspect Biol **2:**a000422. http://dx.doi.org/10.1101/cshperspect.a000422.
6. **Kerfeld CA, Heinhorst S, Cannon GC**. 2010. Bacterial microcompartments. Annu Rev Microbiol **64:**391–408. http://dx.doi.org/10.1146/annurev.micro.112408.134211.
7. **Tucker JD, Siebert CA, Escalante M, Adams PG, Olsen JD, Otto C, Stokes DL, Hunter CN**. 2010. Membrane invagination in Rhodobacter sphaeroides is initiated at curved regions of the cytoplasmic membrane, then forms both budded and fully detached spherical vesicles. Mol Microbiol **76:**833–847. http://dx.doi.org/10.1111/j.1365-2958.2010.07153.x.
8. **Niederman RA**. 2013. Membrane development in purple photosynthetic bacteria in response to alterations in light intensity and oxygen tension. Photosynth Res **116:**333–348. http://dx.doi.org/10.1007/s11120-013-9851-0.
9. **Cameron JC, Wilson SC, Bernstein SL, Kerfeld CA**. 2013. Biogenesis of a bacterial organelle: the carboxysome assembly pathway. Cell **155:** 1131–1140. http://dx.doi.org/10.1016/j.cell.2013.10.044.
10. **Chen AH, Robinson-Mosher A, Savage DF, Silver PA, Polka JK**. 2013. The bacterial carbon-fixing organelle is formed by shell envelopment of preassembled cargo. PLoS One **8:**e76127. http://dx.doi.org/10.1371/journal.pone.0076127.
11. **Savage DF, Afonso B, Chen AH, Silver PA**. 2010. Spatially ordered dynamics of the bacterial carbon fixation machinery. Science **327:** 1258–1261. http://dx.doi.org/10.1126/science.1186090.
12. **Katzmann E, Müller FD, Lang C, Messerer M, Winklhofer M, Plitzko JM, Schüler D**. 2011. Magnetosome chains are recruited to cellular division sites and split by asymmetric septation. Mol Microbiol **82:** 1316–1329. http://dx.doi.org/10.1111/j.1365-2958.2011.07874.x.
13. **Staniland SS, Moisescu C, Benning LG**. 2010. Cell division in magnetotactic bacteria splits magnetosome chain in half. J Basic Microbiol **50:** 392–396. http://dx.doi.org/10.1002/jobm.200900408.
14. **Balkwill DL, Maratea D, Blakemore RP**. 1980. Ultrastructure of a magnetotactic spirillum. J Bacteriol **141:**1399–1408.
15. **Komeili A**. 2012. Molecular mechanisms of compartmentalization and biomineralization in magnetotactic bacteria. FEMS Microbiol Rev **36:** 232–255. http://dx.doi.org/10.1111/j.1574-6976.2011.00315.x.
16. **Schüler D**. 2008. Genetics and cell biology of magnetosome formation in magnetotactic bacteria. FEMS Microbiol Rev **32:**654–672. http://dx.doi.org/10.1111/j.1574-6976.2008.00116.x.
17. **Lefèvre CT, Bazylinski DA**. 2013. Ecology, diversity, and evolution of magnetotactic bacteria. Microbiol Mol Biol Rev **77:**497–526. http://dx.doi.org/10.1128/MMBR.00021-13.
18. **Grünberg K, Müller EC, Otto A, Reszka R, Linder D, Kube M, Reinhardt R, Schüler D**. 2004. Biochemical and proteomic analysis of the magnetosome membrane in Magnetospirillum gryphiswaldense. Appl Environ Microbiol **70:**1040–1050. http://dx.doi.org/10.1128/AEM.70.2.1040-1050.2004.
19. **Tanaka M, Okamura Y, Arakaki A, Tanaka T, Takeyama H, Matsunaga T**. 2006. Origin of magnetosome membrane: proteomic analysis of magnetosome membrane and comparison with cytoplasmic membrane. Proteomics **6:**5234–5247. http://dx.doi.org/10.1002/pmic.200500887.
20. **Matsunaga T, Okamura Y, Fukuda Y, Wahyudi AT, Murase Y, Takeyama H**. 2005. Complete genome sequence of the facultative anaerobic magnetotactic bacterium Magnetospirillum sp. strain AMB-1. DNA Res **12:**157–166. http://dx.doi.org/10.1093/dnares/dsi002.
21. **Lefèvre CT, Trubitsyn D, Abreu F, Kolinko S, Jogler C, de Almeida LG, de Vasconcelos AT, Kube M, Reinhardt R, Lins U, Pignol D, Schüler D, Bazylinski DA, Ginet N**. 2013. Comparative genomic analysis of magnetotactic bacteria from the Deltaproteobacteria provides new insights into magnetite and greigite magnetosome genes required for magnetotaxis. Environ Microbiol **15:**2712–2735. http://dx.doi.org/10.1111/1462-2920.12128.
22. **Quinlan A, Murat D, Vali H, Komeili A**. 2011. The HtrA/DegP family protease MamE is a bifunctional protein with roles in magnetosome protein localization and magnetite biomineralization. Mol Microbiol **80:** 1075–1087. http://dx.doi.org/10.1111/j.1365-2958.2011.07631.x.
23. **Murat D, Quinlan A, Vali H, Komeili A**. 2010. Comprehensive genetic dissection of the magnetosome gene island reveals the step-wise assembly of a prokaryotic organelle. Proc Natl Acad Sci U S A **107:**5593–5598. http://dx.doi.org/10.1073/pnas.0914439107.
24. **Lohsse A, Ullrich S, Katzmann E, Borg S, Wanner G, Richter M, Voigt B, Schweder T, Schüler D**. 2011. Functional analysis of the magnetosome island in Magnetospirillum gryphiswaldense: the mamAB operon is sufficient for magnetite biomineralization. PLoS One **6:**e25561. http://dx.doi.org/10.1371/journal.pone.0025561.
25. **Murat D, Falahati V, Bertinetti L, Csencsits R, Körnig A, Downing K, Faivre D, Komeili A**. 2012. The magnetosome membrane protein, MmsF, is a major regulator of magnetite biomineralization in Magnetospirillum magneticum AMB-1. Mol Microbiol **85:**684–699. http://dx.doi.org/10.1111/j.1365-2958.2012.08132.x.
26. **Rahn-Lee L, Byrne ME, Zhang M, Le Sage D, Glenn DR, Milbourne T, Walsworth RL, Vali H, Komeili A**. 2015. A genetic strategy for probing the functional diversity of magnetosome formation. PLoS Genet **11:** e1004811. http://dx.doi.org/10.1371/journal.pgen.1004811.
27. **Scheffel A, Gruska M, Faivre D, Linaroudis A, Plitzko JM, Schüler D**. 2006. An acidic protein aligns magnetosomes along a filamentous structure in magnetotactic bacteria. Nature **440:**110–114. http://dx.doi.org/10.1038/nature04382.
28. **Komeili A, Vali H, Beveridge TJ, Newman DK**. 2004. Magnetosome vesicles are present before magnetite formation, and MamA is required for their activation. Proc Natl Acad Sci U S A **101:**3839–3844. http://dx.doi.org/10.1073/pnas.0400391101.
29. **Klumpp S, Faivre D**. 2012. Interplay of magnetic interactions and active movements in the formation of magnetosome chains. PLoS One **7:**e33562. http://dx.doi.org/10.1371/journal.pone.0033562.
30. **Topp S, Reynoso CM, Seeliger JC, Goldlust IS, Desai SK, Murat D, Shen A, Puri AW, Komeili A, Bertozzi CR, Scott JR, Gallivan JP**. 2010. Synthetic riboswitches that induce gene expression in diverse bacterial species. Appl Environ Microbiol **76:**7881–7884. http://dx.doi.org/10.1128/AEM.01537-10.
31. **Nudelman H, Zarivach R**. 2014. Structure prediction of magnetosome-associated proteins. Front Microbiol **5:**9. http://dx.doi.org/10.3389/fmicb.2014.00009.
32. **Jensen GJ, Briegel A**. 2007. How electron cryotomography is opening a new window onto prokaryotic ultrastructure. Curr Opin Struct Biol **17:** 260–267. http://dx.doi.org/10.1016/j.sbi.2007.03.002.
33. **Li Z, Jensen GJ**. 2009. Electron cryotomography: a new view into microbial ultrastructure. Curr Opin Microbiol **12:**333–340. http://dx.doi.org/10.1016/j.mib.2009.03.007.
34. **Rudner DZ, Losick R**. 2010. Protein subcellular localization in bacteria. Cold Spring Harb Perspect Biol **2:**a000307. http://dx.doi.org/10.1101/cshperspect.a000307.
35. **Komeili A, Li Z, Newman DK, Jensen GJ**. 2006. Magnetosomes are cell membrane invaginations organized by the actin-like protein MamK. Science **311:**242–245. http://dx.doi.org/10.1126/science.1123231.
36. **Draper O, Byrne ME, Li Z, Keyhani S, Barrozo JC, Jensen G, Komeili A**. 2011. MamK, a bacterial actin, forms dynamic filaments in vivo that are regulated by the acidic proteins MamJ and LimJ. Mol Microbiol **82:** 342–354. http://dx.doi.org/10.1111/j.1365-2958.2011.07815.x.
37. **Ozyamak E, Kollman J, Agard DA, Komeili A**. 2013. The bacterial actin

MamK: in vitro assembly behavior and filament architecture. J Biol Chem **288:**4265–4277. http://dx.doi.org/10.1074/jbc.M112.417030.
38. **Ding Y, Li J, Liu J, Yang J, Jiang W, Tian J, Li Y, Pan Y, Li J.** 2010. Deletion of the ftsZ-like gene results in the production of superparamagnetic magnetite magnetosomes in Magnetospirillum gryphiswaldense. J Bacteriol **192:**1097–1105. http://dx.doi.org/10.1128/JB.01292-09.
39. **Müller FD, Raschdorf O, Nudelman H, Messerer M, Katzmann E, Plitzko JM, Zarivach R, Schüler D.** 2014. The FtsZ-like protein FtsZm of Magnetospirillum gryphiswaldense likely interacts with its generic homolog and is required for biomineralization under nitrate deprivation. J Bacteriol **196:**650–659. http://dx.doi.org/10.1128/JB.00804-13.
40. **Rioux JB, Philippe N, Pereira S, Pignol D, Wu LF, Ginet N.** 2010. A second actin-like MamK protein in Magnetospirillum magneticum AMB-1 encoded outside the genomic magnetosome island. PLoS One **5:**e9151. http://dx.doi.org/10.1371/journal.pone.0009151.
41. **Mann HB, Whitney DR.** 1947. On a test of whether one of two random variables is stochastically larger than the other. Ann Math Stat **18:**50–60. http://dx.doi.org/10.1214/aoms/1177730491.
42. **Chan Y-HM, Marshall WF.** 2012. How cells know the size of their organelles. Science **337:**1186–1189. http://dx.doi.org/10.1126/science.1223539.
43. **Yamamoto A, DeWald DB, Boronenkov IV, Anderson Ra, Emr SD, Koshland D.** 1995. Novel PI(4)P 5-kinase homologue, Fab1p, essential for normal vacuole function and morphology in yeast. Mol Biol Cell **6:**525–539.
44. **Katzmann E, Scheffel A, Gruska M, Plitzko JM, Schüler D.** 2010. Loss of the actin-like protein MamK has pleiotropic effects on magnetosome formation and chain assembly in Magnetospirillum gryphiswaldense. Mol Microbiol **77:**208–224. http://dx.doi.org/10.1111/j.1365-2958.2010.07202.x.
45. **McMahon HT, Gallop JL.** 2005. Membrane curvature and mechanisms of dynamic cell membrane remodelling. Nature **438:**590–596. http://dx.doi.org/10.1038/nature04396.
46. **Mim C, Unger VM.** 2012. Membrane curvature and its generation by BAR proteins. Trends Biochem Sci **37:**526–533. http://dx.doi.org/10.1016/j.tibs.2012.09.001.
47. **Stachowiak JC, Hayden CC, Sasaki DY.** 2010. Steric confinement of proteins on lipid membranes can drive curvature and tubulation. Proc Natl Acad Sci U S A **107:**7781–7786. http://dx.doi.org/10.1073/pnas.0913306107.
48. **McMahon HT, Boucrot E.** 2011. Molecular mechanism and physiological functions of clathrin-mediated endocytosis. Nat Rev Mol Cell Biol **12:**517–533. http://dx.doi.org/10.1038/nrm3151.
49. **Shibata Y, Shemesh T, Prinz WA, Palazzo AF, Kozlov MM, Rapoport TA.** 2010. Mechanisms determining the morphology of the peripheral ER. Cell **143:**774–788. http://dx.doi.org/10.1016/j.cell.2010.11.007.
50. **Rafelski SM.** 2013. Mitochondrial network morphology: building an integrative, geometrical view. BMC Biol **11:**71. http://dx.doi.org/10.1186/1741-7007-11-71.
51. **Baumgart T, Capraro BR, Zhu C, Das SL.** 2011. Thermodynamics and mechanics of membrane curvature generation and sensing by proteins and lipids. Annu Rev Phys Chem **62:**483–506. http://dx.doi.org/10.1146/annurev.physchem.012809.103450.
52. **Tanaka M, Arakaki A, Matsunaga T.** 2010. Identification and functional characterization of liposome tubulation protein from magnetotactic bacteria. Mol Microbiol **76:**480–488. http://dx.doi.org/10.1111/j.1365-2958.2010.07117.x.
53. **Govindarajan S, Nevo-Dinur K, Amster-Choder O.** 2012. Compartmentalization and spatio-temporal organization of macromolecules in bacteria. FEMS Microbiol Rev **36:**1005–1022. http://dx.doi.org/10.1111/j.1574-6976.2012.00348.x.
54. **Butler RF, Banerjee SK.** 1975. Theoretical single-domain grain size range in magnetite and titanomagnetite. J Geophys Res **80:**4049–4058. http://dx.doi.org/10.1029/JB080i029p04049.
55. **Schneider CA, Rasband WS, Eliceiri KW.** 2012. NIH image to ImageJ: 25 years of image analysis. Nat Methods **9:**671–675. http://dx.doi.org/10.1038/nmeth.2089.
56. **Kremer JR, Mastronarde DN, McIntosh JR.** 1996. Computer visualization of three-dimensional image data using IMOD. J Struct Biol **116:**71–76. http://dx.doi.org/10.1006/jsbi.1996.0013.
57. **Mastronarde D.** 2006. Fiducial marker and hybrid alignment methods for single- and double-axis tomography, p 163–185. In Frank J (ed), Electron tomography. Springer, New York, NY.
58. **Iancu CV, Tivol WF, Schooler JB, Dias DP, Henderson GP, Murphy GE, Wright ER, Li Z, Yu Z, Briegel A, Gan L, He Y, Jensen GJ.** 2006. Electron cryotomography sample preparation using the Vitrobot. Nat Protoc **1:**2813–2819. http://dx.doi.org/10.1038/nprot.2006.432.
59. **Tivol WF, Briegel A, Jensen GJ.** 2008. An improved cryogen for plunge freezing. Microsc Microanal **14:**375–379. http://dx.doi.org/10.1017/S1431927608080781.
60. **Zheng SQ, Keszthelyi B, Branlund E, Lyle JM, Braunfeld MB, Sedat JW, Agard DA.** 2007. UCSF tomography: an integrated software suite for real-time electron microscopic tomographic data collection, alignment, and reconstruction. J Struct Biol **157:**138–147. http://dx.doi.org/10.1016/j.jsb.2006.06.005.